Collective Motion of Methylammonium Cations Affects Phase Transition and Self-Trapped Exciton Emission in MAPbI$_3$ Films

Chia-Hsun Yeh,[1] Wen-Yu Cheng,[2] Tai-Che Chou,[1] Yi-Chun Liu,[1] Chia-Wei Chang,[1] Yu-Sheng Chen,[3] Chih-Hsing Wang,[1] Shih-Chang Weng,[3] Ian D. Sharp,[2,*] Pi-Tai Chou,[1,4] Chang-Ming Jiang[1,4,*]

[1]Department of Chemistry, National Taiwan University, 10617 Taipei, Taiwan

[2]Walter Schottky Institute, Technical University of Munich, 85748 Garching, Germany

[3]National Synchrotron Radiation Research Center, 300092 Hsinchu, Taiwan

[4]Center for Emerging Materials and Advanced Devices, National Taiwan University, 10617 Taipei, Taiwan

*Corresponding Authors: sharp@wsi.tum.de, cmjiang@ntu.edu.tw

ABSTRACT

Hybrid organic-inorganic halide perovskites are celebrated for their exceptional optoelectronic properties and facile fabrication methods, making them prime candidates for next-generation photovoltaic and optoelectronic devices. However, their inherent instability limits practical applications. To address this, a new class of 3D hollow perovskites, denoted as {*en*}MAPbI$_3$, has been developed by partially replacing methylammonium (MA$^+$) with ethylenediammonium (*en*) cations. This study systematically investigates the structural, phase transition, and photophysical properties of {*en*}MAPbI$_3$ thin films with varying *en* content. Incorporating *en* cations expands the unit cell, suppresses the tetragonal-to-orthorhombic phase transition, and disrupts dipole-dipole interactions among MA$^+$ cations. Temperature-dependent photoluminescence (PL) and X-ray diffraction (XRD) reveal that *en* incorporation stabilizes the tetragonal phase while diminishing the collective rotational dynamics of MA$^+$ cations, crucial for phase stability and self-trapped exciton (STE) formation. These insights advance the understanding of 3D hollow perovskites and highlight their potential for stable and tunable optoelectronic applications.

▪ INTRODUCTION

Hybrid organic-inorganic halide perovskites, such as methylammonium lead iodide (MAPbI$_3$), have emerged as promising materials for next-generation optoelectronic devices due to their exceptional properties, including long carrier lifetimes, high absorption coefficients, tunable band gaps, and intrinsic defect tolerance.[1-5] These attributes have propelled the power conversion efficiencies (PCEs) of single-junction perovskite solar cells to exceed 25%.[6-8] However, the inherent instability of halide perovskites under ambient conditions, primarily driven by the volatility of organic cations, remains a critical challenge for their large-scale deployment.[9-11] Efforts to replace the toxic Pb^{2+} with Sn^{2+} exacerbate these instability issues and lead to much lower achievable PCEs.[12]

To address these limitations, a new family of "3D hollow perovskites," described by the general formula $(A)_{1-x}(L)_xBX_3$ has been recently introduced. In these systems, larger organic cations (L) such as ethylenediammonium (en^{2+}) and hydroxyethylammonium (HEA$^+$) partially replace methylammonium (MA$^+$) or formamidinium (FA$^+$) at the A-site, with B = Pb^{2+} or Sn^{2+}, and X = Br$^-$ or I$^-$.[13-23] These materials exhibit enhanced air and photostability, alongside improved photovoltaic performances, in both Pb- and Sn-based systems. The incorporation of larger organic cations modifies the perovskite crystal structure in two key ways: (1) unit cell expansion, sometimes inducing phase transition as governed by the Goldschmidt tolerance factor,[24,25] and (2) the creation of vacancies at the B-site and halide positions to accommodate the larger cations, forming a robust 3D hollow framework.[16,26-28] These structural changes not only improve material stability but also tune optoelectronic properties, such as widening the optical bandgaps and extending carrier lifetimes, despite the introduction of additional vacancy defects.[15,18,19] Nevertheless, the fundamental mechanisms by which these larger cations influence carrier dynamics and excitonic behavior remain elusive.

The dynamic behavior of A-site cations, possessing anisotropic sizes and roles as hydrogen bond donors, plays a pivotal role in determining the structural and optoelectronic properties of hybrid halide perovskites.[29-31] Despite the absence of covalent bonding between organic cations and the inorganic components, A-site cations, such as MA$^+$, significantly influence phase transitions and excitonic behavior through their rotational dynamics and dipole interactions. For example, MAPbI$_3$ undergoes distinct phase transitions – from cubic to tetragonal to orthorhombic phases – as the temperatures decrease, reflected by the tilting of [PbI$_6$] octahedra.[32-35] At low temperatures, the diminished rotational degrees of freedom of MA$^+$ result in organized domains through dipole-dipole interaction among MA$^+$. These interactions, alongside hydrogen bonding between MA$^+$ and I$^-$, drive lattice distortions and phase transitions.[30] Using the neutron scattering technique, Yu et al. have identified that the isotropic orientation of formamidinium (FA$^+$) in FAPbI$_3$

3

https://doi.org/10.26434/chemrxiv-2024-j7bb2-v2 **ORCID:** https://orcid.org/0000-0001-8327-5760 Content not peer-reviewed by ChemRxiv. **License:** CC BY-NC-ND 4.0

▪ INTRODUCTION

Hybrid organic-inorganic halide perovskites, such as methylammonium lead iodide (MAPbI$_3$), have emerged as promising materials for next-generation optoelectronic devices due to their exceptional properties, including long carrier lifetimes, high absorption coefficients, tunable band gaps, and intrinsic defect tolerance.[1-5] These attributes have propelled the power conversion efficiencies (PCEs) of single-junction perovskite solar cells to exceed 25%.[6-8] However, the inherent instability of halide perovskites under ambient conditions, primarily driven by the volatility of organic cations, remains a critical challenge for their large-scale deployment.[9-11] Efforts to replace the toxic Pb^{2+} with Sn^{2+} exacerbate these instability issues and lead to much lower achievable PCEs.[12]

To address these limitations, a new family of "3D hollow perovskites," described by the general formula $(A)_{1-x}(L)_xBX_3$ has been recently introduced. In these systems, larger organic cations (L) such as ethylenediammonium (en^{2+}) and hydroxyethylammonium (HEA$^+$) partially replace methylammonium (MA$^+$) or formamidinium (FA$^+$) at the A-site, with B = Pb^{2+} or Sn^{2+}, and X = Br$^-$ or I$^-$.[13-23] These materials exhibit enhanced air and photostability, alongside improved photovoltaic performances, in both Pb- and Sn-based systems. The incorporation of larger organic cations modifies the perovskite crystal structure in two key ways: (1) unit cell expansion, sometimes inducing phase transition as governed by the Goldschmidt tolerance factor,[24,25] and (2) the creation of vacancies at the B-site and halide positions to accommodate the larger cations, forming a robust 3D hollow framework.[16,26-28] These structural changes not only improve material stability but also tune optoelectronic properties, such as widening the optical bandgaps and extending carrier lifetimes, despite the introduction of additional vacancy defects.[15,18,19] Nevertheless, the fundamental mechanisms by which these larger cations influence carrier dynamics and excitonic behavior remain elusive.

The dynamic behavior of A-site cations, possessing anisotropic sizes and roles as hydrogen bond donors, plays a pivotal role in determining the structural and optoelectronic properties of hybrid halide perovskites.[29-31] Despite the absence of covalent bonding between organic cations and the inorganic components, A-site cations, such as MA$^+$, significantly influence phase transitions and excitonic behavior through their rotational dynamics and dipole interactions. For example, MAPbI$_3$ undergoes distinct phase transitions – from cubic to tetragonal to orthorhombic phases – as the temperatures decrease, reflected by the tilting of [PbI$_6$] octahedra.[32-35] At low temperatures, the diminished rotational degrees of freedom of MA$^+$ result in organized domains through dipole-dipole interaction among MA$^+$. These interactions, alongside hydrogen bonding between MA$^+$ and I$^-$, drive lattice distortions and phase transitions.[30] Using the neutron scattering technique, Yu et al. have identified that the isotropic orientation of formamidinium (FA$^+$) in FAPbI$_3$

in the high-temperature cubic phase is frozen to a more ordered arrangement in the low-temperature tetragonal phase, which also signifies the interplay between organic cation rotational dynamics and the inorganic framework.[36] Recent studies have also demonstrated that the structural dynamics in hybrid halide perovskites facilitate self-trapped exciton (STE) formation through strong electron-phonon coupling, a characteristic feature of highly ionic halide perovskites.[37-40] Unlike free excitons, which recombine rather rapidly, STEs are stabilized by lattice distortions, resulting in prolonged carrier lifetimes and broadband emission.[40-42] However, the extent to which A-site cation rotational dynamics influence STE formation and phase stability dynamics is still poorly understood.

Motivated by these challenges, this study investigates the structural, phase transition, and photophysical properties of 3D hollow {*en*}MAPbI$_3$ thin films with varying *en* content. The much lower static dipole moment of *en*$^{2+}$ compared to MA$^+$ disrupts long-range dipole-dipole interactions among A-site cations, which alters phase transitions and carrier recombination dynamics. Using temperature-dependent photoluminescence (PL) and X-ray diffraction (XRD), we reveal how *en* incorporation suppresses the tetragonal-to-orthorhombic (TP-to-OP) phase transition and reduces the intensity and Stokes shift of STE emission at low temperatures. These insights bridge the gap between structural dynamics and carrier behavior in hybrid halide perovskites, offering a pathway for optimizing them for photovoltaic and light-emitting diode applications.

▪ **EXPERIMENTAL METHODS**

Synthesis of {*en*}MAPbI$_3$ films. All films were prepared on amorphous SiO$_2$ substrates (1 × 1 cm^2) using a one-step spin-coating procedure in a nitrogen-filled glove box (**Figure S1**). For pristine MAPbI$_3$, a precursor solution was prepared by dissolving 0.8 mmol of methylammonium iodide (CH$_3$NH$_3$I, >99%, TCI) and 0.8 mmol of lead (II) iodide (PbI$_2$, 99.999%, Alfa Aesar) in 1.00 mL of a 4:1 (v/v) DMF/DMSO mixture. {*en*}MAPbI$_3$ films were prepared by partially replacing CH$_3$NH$_3$I with ethane-1,2-diammonium iodide at the specified stoichiometric ratio to achieve *en* substitution of 5.0, 7.5, 10.0, and 15.0% (see Supporting Information for full details).

The amorphous SiO$_2$ substrates were cleaned sequentially in an ultrasonic bath with deionized water (10 minutes, twice), acetone (20 minutes), and isopropanol (20 minutes). After drying with a nitrogen stream and in an oven, the substrates were treated in a UV-ozone cleaner for 20 minutes. The spin-coating process was performed using 10 µL of precursor solution at 4000 rpm for 30 seconds, with an acceleration rate of 800 rpm/s. During the spin-coating process, 100 µL of chlorobenzene (anhydrous, 99.9%, Sigma-Aldrich) anti-solvent was dropped onto the rotating substrate 3 seconds before the end of the process. The as-coated films were annealed on a hotplate

4

at specified temperatures for 10 minutes. A protective layer was applied by spin-coating 15 µL of a 10 mg/mL poly(methyl methacrylate) solution in chlorobenzene at 5000 rpm for 35 seconds (800 rpm/s acceleration rate), followed by annealing at 80°C for 10 minutes.

Powder X-ray diffraction (PXRD). Room-temperature PXRD patterns were obtained using a PANalytical X'Pert PRO diffractometer equipped with a Cu anode ($\lambda_{K\alpha}$ = 1.54178 Å) over a 2θ range of 5 – 50°. Temperature-dependent XRD measurements were conducted at Beamline 09A of the Taiwan Photon Source, National Synchrotron Radiation Research Center. The thin-film sample was placed in a closed-cycle helium cryostat mounted on the Eulerian cradle of a 9-circle diffractometer; a scintillation detector on the 2θ arm was used for XRD measurement using 12 keV (λ = 1.0332 Å) X-ray energy. The sample temperature was controlled between 20 – 300 K, with a stabilization time of 15 minutes at each temperature point.

Steady-state and time-resolved optical characterizations. Ultraviolet-visible (UV-Vis) transmission spectra of MAPbI$_3$ films were recorded in the range of 400 – 1200 nm using a spectrophotometer (UH-5700, Hitachi), with a bare amorphous SiO$_2$ substrate in the reference beam path. Photoluminescence (PL) spectra were measured using an FLS 980 fluorimeter (Edinburgh Instruments) equipped with a photomultiplier detector and a 510 nm pulsed diode laser as the excitation source. The temporal evolution of PL intensity was analyzed using the time-correlated single photon counting (TCSPC) technique. The instrument response function, obtained with an aluminum foil at the sample mount, was deconvoluted from the time-resolved PL traces.

For low-temperature PL measurements, the thin-film samples were mounted in a closed-cycle helium cryostat (CS202-DMX-1AL, Advanced Research Systems, Inc.) evacuated by a turbomolecular pump. A thermocouple installed on the cold finger of the cryostat was connected to a temperature controller (Model 350, Lake Shore), which modulated the sample temperature between 10 – 300 K using an integrated resistive heater.

▪ **RESULTS AND DISCUSSION**

Structural Analysis of {*en*}MAPbI$_3$ Films

The structural properties of {*en*}MAPbI$_3$ thin films with 0 – 15 % *en* incorporations were investigated via PXRD. As shown in **Figure 1a**, all diffraction peaks below 10% *en* loading can be indexed to the tetragonal perovskite structure (TP; space group $I4/mcm$). Two trends were observed with increasing *en* loading: (1) a monotonic shift of diffraction peaks toward smaller 2θ angles, indicating unit cell expansion due to the incorporation of larger *en* cations, consistent with prior reports of {*en*}MAPbI$_3$[33,35,39] and similar hollow hybrid halide perovskites;[16] and (2) reduced

5

diffraction intensities, which suggest disruption in long-range crystallographic order arising from the random distribution of *en* and the resulting point defects.

Notably, the substitution of MA^+ cations with larger *en* cations can introduce a risk of forming quasi-2D MAPbI₃ domains, similar to when organic cations with longer alkyl chains are present in the synthesis.[21,24] The quasi-2D MAPbI₃ is characterized by additional diffraction peaks at 2θ < 10º. However, our optimized synthesis conditions successfully minimize such domains, as evidenced by the absence of these peaks and PbI_2 impurities in the PXRD patterns (see Supporting Information for details). These results confirm the successful preparation of 3D hollow {*en*}MAPbI₃ films.

Interestingly, the (211) diffraction peak of tetragonal MAPbI₃ weakens at 10% *en* loading and disappears entirely at 15% *en* loading, signaling a phase transition to the cubic perovskite phase (CP; space group $Pm\overline{3}m$). This transition aligns with the prediction from the Goldschmidt tolerance factor and previous reports,[16,43] indicating that incorporating larger *en* cations stabilizes the cubic structure at room temperature.
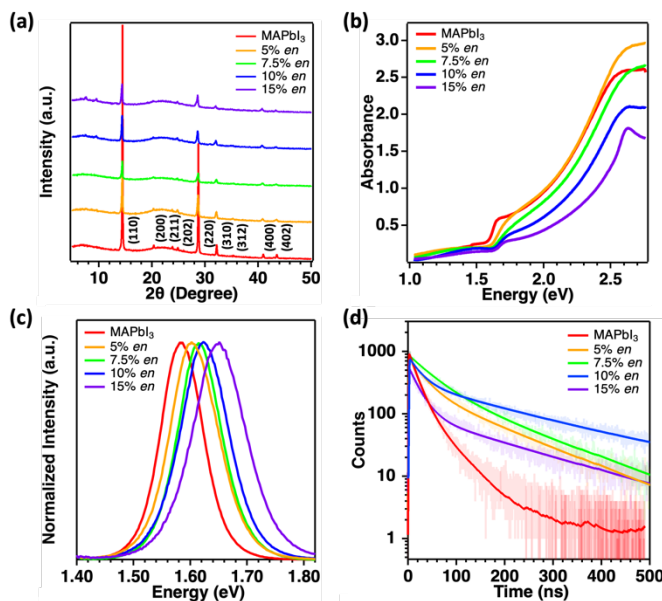
Figure 1. (a) PXRD patterns, (b) UV-Vis absorption spectra, (c) room-temperature steady-state PL spectra, and (d) time-resolved PL traces measured from {*en*}MAPbI₃ films with different *en* loadings. The solid lines in panel (d) represent the fitting results using a bi-exponential model.

Photophysical Properties and Carrier Dynamics

The UV-Vis absorption spectra of {*en*}MAPbI₃ films (**Figure 1b**) reveal a systematic blueshift in the absorption onset with increasing *en* loading. Room-temperature PL spectra (**Figure 1c**), recorded under 510 nm (hν = 2.43 eV) excitation, show a single emission peak attributed to

6

the radiative recombination of free carriers.[44] This PL peak shifts from 1.58 eV for pristine MAPbI$_3$ to 1.65 eV for the 15% *en* sample, reflecting a widening of the optical bandgap. The bandgap widening can be attributed to the Pb 6*s*–I 5*p* anti-bonding nature of the valence band maximum (VBM), which decreases in energy with lattice expansion, while the conduction band minimum (CBM), having non-bonding character, remains unaffected.[39,45] These results confirm that *en* incorporation not only modifies the structural properties of MAPbI$_3$ but also tunes its optoelectronic properties.

Time-correlated single-photon counting (TCSPC) measurements provided insights into carrier dynamics of {*en*}MAPbI$_3$ films (**Figure 1d**). PL decay traces were fitted using a bi-exponential model:

$$I(t) = A_0 + A_1 \exp\left(-\frac{t}{\tau_1}\right) + A_2 \exp\left(-\frac{t}{\tau_2}\right) \qquad (1)$$

where A_0 is the background level, A_i is the weight factor for each decay channel, and τ_i is the decay time. Here, τ_1 represents Schottky-Read-Hall recombination mediated by defect states, while τ_2 corresponds to radiative recombination of free carriers at room temperature.[44,46] The fitting results (**Table 1**) reveal a significant increase in τ_2 with *en* loading, except for the 15% *en* sample, where the trend reverses. Concurrently, the ratio $A_1/(A_1 + A_2)$ decreases from 0.80 for pristine MAPbI$_3$ to 0.62 for the 10% *en* sample, indicating suppression of defect-mediated non-radiative recombination pathways in 3D hollow {*en*}MAPbI$_3$. The intensity-weighted average PL lifetime (τ_{avg}) was calculated as:

$$\tau_{avg} = \frac{A_1\tau_1^2 + A_2\tau_2^2}{A_1\tau_1 + A_2\tau_2} \qquad (2)$$

Here, τ_{avg} increased from 30.52 ns for pristine MAPbI$_3$ to 171.98 ns for the 10% *en* film, consistent with prolonged carrier lifetimes observed in structurally similar {*en*}FASnI$_3$, {*en*}FA$_{0.5}$MA$_{0.5}$Pb$_{0.5}$Sn$_{0.5}$I$_3$, and {*en*}MASnI$_3$ films.[14,18,19] At high *en* loadings, however, the emergence of the cubic MAPbI$_3$ phase disrupts these trends, as evidenced by shortened τ_{avg} (127.03 ns) for the 15% *en* film.[32]

We also managed to synthesize an {*en*}MAPbI$_3$ film with 10% of MA$^+$ replaced by *en* in the precursor solution. This film uniquely exhibited a CP diffraction pattern, and the room-temperature PL shifted notably to 1.71 eV (**Figure S5**). Furthermore, τ_{avg} decreased drastically to 15.02 ns for this film, which is in line with the expected behavior of the CP phase. These observations imply that the extent of *en* incorporation in this film, hereafter denoted as 10% *en*(CP), is much higher than other {*en*}MAPbI$_3$ films. Even though attempts to reproduce the synthesis have turned out to be unsuccessful, we will still analyze the temperature-dependent PL and XRD results of 10% *en*(CP) and compare them with other films in later paragraphs.

Table 1. Fitting results for the time-resolved PL traces monitored at respective peak PL emission energies of {*en*}MAPbI$_3$ films with varying *en* loadings.

Samples	τ_1 (ns)	A_1	τ_2 (ns)	A_2	τ_{avg} (ns)	$A_1/(A_1 + A_2)$
MAPbI$_3$	16.50	0.082	49.63	0.020	30.52	0.80
5% *en*	29.38	0.188	136.88	0.084	102.00	0.69
7.5% *en*	46.93	0.197	148.41	0.096	108.47	0.67
10% *en*	23.72	0.071	200.89	0.043	171.98	0.62
15% *en*	21.66	0.157	185.55	0.033	127.03	0.83

Phase Transition Behaviors

Temperature-dependent PL measurements on {*en*}MAPbI$_3$ (**Figure 2**) reveal spectral redshifts as the temperature decreases from 300 K, which can be attributed to unit cell contraction elevating the Pb–I anti-bonding energy levels at the VBM.[47] For pristine MAPbI$_3$, a sudden blueshift in PL at 150 K corresponds to the TP-to-OP transition, during which the tilting of [PbI$_6$] octahedra weakens the interaction between Pb^{2+} and I$^-$. Increasing *en* loading was found to lower the phase transition temperature to 130 K, 120 K, and 100 K for films with 5%, 10%, and 15% *en*, respectively, suggesting enhanced TP stability due to *en* incorporation.
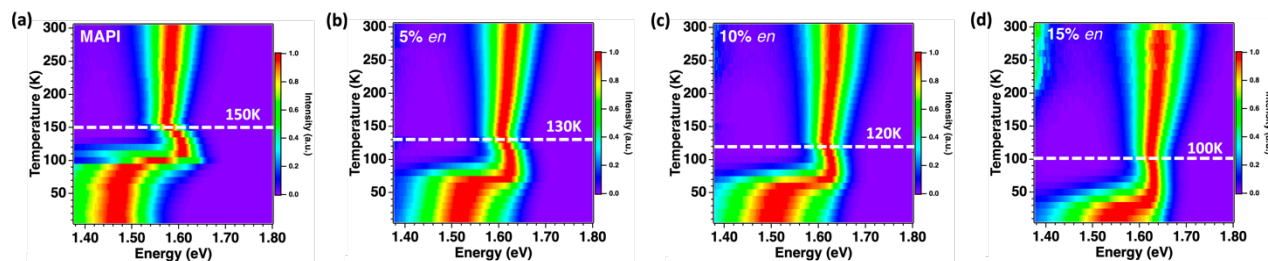
Figure 2. Temperature-dependent PL spectra of (a) pristine MAPbI$_3$ and {*en*}MAPbI$_3$ films with (b) 5%, (c) 10%, and (d) 15% *en* loading. The tetragonal-to-orthorhombic phase transition temperatures are marked with dashed lines.

For the 10% *en*(CP) film with the greatest extent of *en* incorporation, no clear signs of phase transition were observed in the temperature-dependent PL study between $100-300$K (**Figure S5d**). However, slight high-energy PL broadening below 100K hints at certain changes to the electronic structure in that temperature range. Temperature-dependent XRD was conducted on a pristine MAPbI$_3$ film and the 10% *en*(CP) film to provide further evidence for the TP-to-OP transition (**Figure S6**). Here, the (110) diffraction of TP and the (101) diffraction of OP were fitted using a Voigt function, and their peak positions were plotted as functions of temperature. In general, the

8

diffraction peaks shifted to lower 2θ angles as the temperature increased, reflecting the dilated unit cell. For pristine MAPbI$_3$, a distinct change in diffraction peak slopes between $130-170$K verified the TP-to-OP phase transition. In contrast, the 10% *en*(CP) film displayed no discernible phase transition within the $100-300$K range, collaborating the temperature-dependent PL measurement.

Based on the temperature-dependent PL and XRD results, we found the phase transition of MAPbI$_3$ between TP and OP rendered to the lower temperature as the *en* loading in 3D hollow perovskite increases. We theorize that this phenomenon originates from the smaller molecular dipole moment of *en* cation compared to MA$^+$. Prior computational studies on MAPbI$_3$ have revealed that the dipole-dipole interaction gives rise to an ordered arrangement of MA$^+$ cations, which is the primary driving force of the TP-to-OP phase transition at low temperatures.[30] The random incorporation of the less polar *en* in A-site would disrupt such collective motion of MA$^+$, and consequently, further reduction in the lattice temperature is required for enlarging the region with MA$^+$ ordering so that phase transition to OP can initiate.

Electron-Phonon Coupling in {*en*}MAPbI$_3$

The full widths of half maximum (FWHMs) of PL emissions in the TP temperature range were analyzed to provide insights into the coupling between electrons and longitudinal optical (LO) phonons, as well as the intrinsic disorder in {*en*}MAPbI$_3$ (**Figure 3**). In the weak electron-phonon coupling regime, the temperature-dependent PL linewidth ($\Gamma(T)$) can be described by:

$$\Gamma(T) = \Gamma_0 + \gamma_{LO}\frac{1}{e^{\frac{E_{LO}}{k_B T}}-1} \qquad (3)$$

where Γ_0 represents the intrinsic linewidth, and E_{LO} and γ_{LO} stand for the energy and coupling constant associated with the LO phonons, respectively.[48,49] As the LO phonon energy of MAPbI$_3$ has not yet been reported, we fixed E_{LO} at 11.5 meV, a value previously extracted from FAPbI$_3$.[48] Fitting results (**Table 2**) reveal consistent 17-22 meV electron-phonon coupling strength across all films. However, Γ_0 can be seen to increase progressively with *en* loading, confirming greater lattice disorder in 3D hollow {*en*}MAPbI$_3$ films.
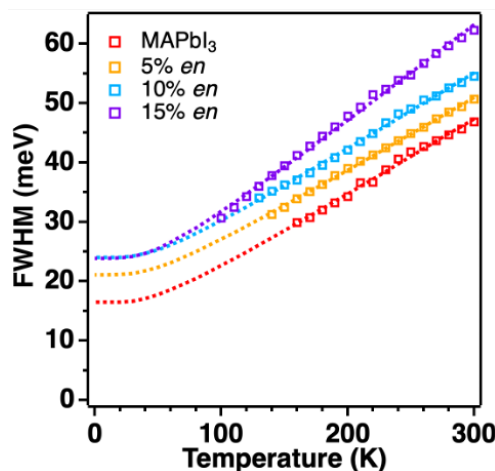
Figure 3. The change of PL linewidths of {*en*}MAPbI₃ films as functions of temperature. Dashed lines represent the fitting results using the weak electron-phonon coupling limit, as described in the main text.

Table 2. List of intrinsic PL linewidth Γ_0 and electron-phonon coupling strength γ_{LO} for {*en*}MAPbI₃ films with different *en* loadings.

Samples	Γ_0 (meV)	γ_{LO} (meV)	E_{LO} (meV)
MAPbI₃	16.5 ± 0.53	17.3 ± 0.40	
5% *en*	21.1 ± 0.18	16.7 ± 0.14	
10% *en*	24.0 ± 0.30	17.4 ± 0.24	11.5
15% *en*	23.9 ± 0.34	22.0 ± 0.30	

Self-Trapped Exciton (STE) Formation

Another observation from the temperature-dependent PL spectra worthy of addressing is the emergence of a broadband emission way below the TP-to-OP transition temperature, especially for the pristine MAPbI₃ film. The large Stokes shift of this emission feature precludes its origin from being free excitons, which typically exhibit < 20 meV binding energy in MAPbI₃ single crystals and thin films.[50,51] Instead, most literature assigned this low-temperature PL of MAPbI₃ in two different ways: defect-related PL or self-trapped exciton.[40,52] In order to differentia these two radiative recombination pathways, we performed excitation power-dependent PL measurements for the pristine MAPbI₃ film at 160 K, when free carrier recombination contributes to the PL, and 10 K when the broadband emission with large Stokes shift dominates. As shown in **Figure 4**, the integrated PL emission intensity of both features exhibited a linearly increasing relationship to the excitation laser power. The defect-related emission, of which the intensity is proportional to the defect sites populated by the photoexcited electrons, would reach a saturation intensity at higher

10

excitation power densities. Furthermore, **Figure 2** reveals that as the *en* loading increased in 3D hollow {*en*}MAPbI$_3$, the temperature at which the broadband emission feature appears became lower, alongside reduced Stokes shifts. The comparison of PL spectra of {*en*}MAPbI$_3$ at 10 K reveals a monotonic blueshift with increasing *en* content (**Figure S7**), though it is unlikely that the radiative defect energy levels in MAPbI$_3$ would exhibit this kind of substantial shift. Therefore, we conclude that the broad emission at lower temperatures originated from the self-trapped exciton (STE) in the OP phase rather than PL-active defects.
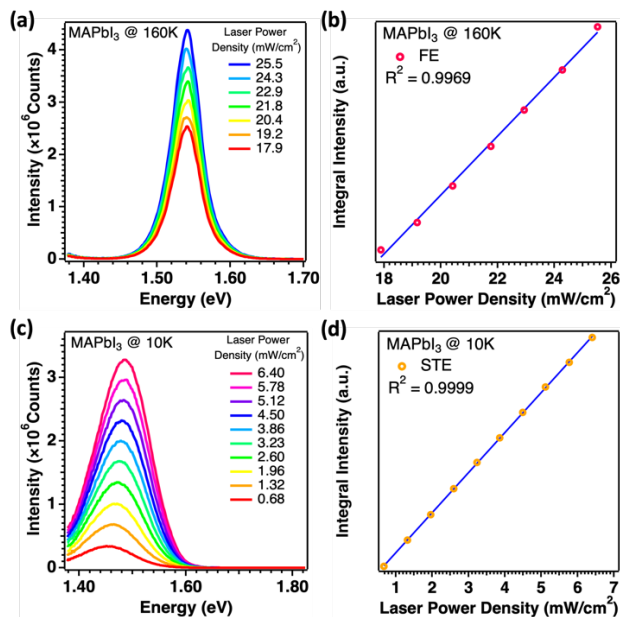
Figure 4. Steady-state PL spectra measured from a pristine MAPbI$_3$ film at (a) 160 K and (c) 10 K using different excitation power from a 510 nm laser. The integrated free exciton (FE) and self-trapped exciton (STE) PL emission intensities are plotted against the excitation power and plotted in (b) and (d), respectively.

The formation of the self-trapped exciton (STE) involves the localization of a free exciton (FE) and the distortion of the surrounding lattice. Here, we posit that the driving force for STE formation involves primarily the collective motion of MA$^+$ surrounding the exciton rather than the inorganic [PbI$_6$] framework. As illustrated in **Figure 5a**, the FE emission still dominates right below the TP-to-OP phase transition temperature, and the dipoles of MA$^+$ are aligned in the same plane but antiparallel to the adjacent MAPbI$_3$ layer, as found in the molecular dynamic simulation.[30] At lower temperatures, however, the MA$^+$ cations surrounding the FE would rearrange to accommodate the exciton's dipole moment. Subsequently, distortions in the corner-sharing [PbI$_6$] octahedral units respond to the realignment of MA$^+$ cations, forming a self-trapped exciton. This phenomenon is analogous to the reorganization of polar solvent molecules around charged species to attain a new equilibrium configuration with lower free energy. In this regard, a

11

greater displacement in the collective nuclear coordinate corresponds to a high extent of energy stabilization, manifesting in a larger Stokes shift for the STE emission relative to FE emission. **Figure 5b** reveals that the peak position of STE emission of pristine MAPbI$_3$ shifts to higher energy as excitation power increases, underscoring the varying configurational energy stabilization through STE formation. The steady-state PL of the 7.5% *en* film at 10 K also displayed a similar blueshift with increasing excitation power density (**Figure S8**). With low excitation power, each FE can exert influence on more MA$^+$ cations and induce extensive lattice distortion, hence resulting in a relatively large Stokes shift. Conversely, higher excitation power creates a larger density of FE such that the average size of STE is restricted, leading to smaller energy stabilization.
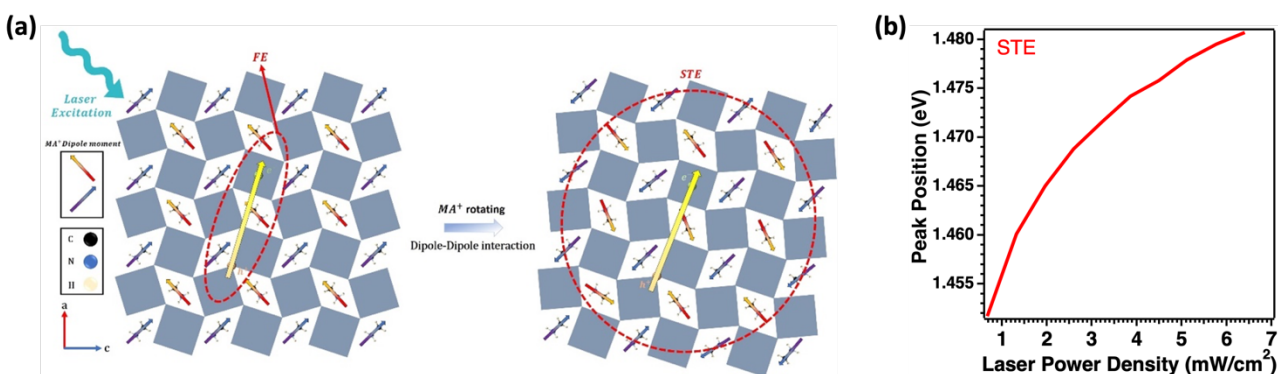
Figure 5. (a) Illustrative diagram for the formation of self-trapped exciton through the collective rearrangement of methylammonium cations in MAPbI$_3$. (b) The shift of STE emission peak position in pristine MAPbI$_3$ film at 10 K with respect to the excitation power density.

Figure 6a depicts the PL spectrum of pristine MAPbI$_3$ at 90 K. Here, three Gaussian peaks can be deconvoluted, which correspond to one FE and two STE emissions. TCSPC measurements were conducted to measure the temporal evolution at 780 nm and 850 nm (**Figure 6b** and **6c**). Here, the FE emission exhibited a much faster decay than the STE emission. More importantly, the rise of STE emission coincided with the fast decay component of the FE emission in the few nanosecond timescale, signifying the collective rotational dynamics of MA$^+$ cations. For the {*en*}MAPbI$_3$ film with 7.5% *en* loading, the steady-state PL spectrum at 90 K also consists of one FE and two STE emission features, though individual components are blue-shifted compared to the pristine MAPbI$_3$ (**Figure 6d**). Similarly, the decay of the PL trace at 770 nm, with a major contribution from FE emission, matches the rise time of the STE-dominant PL trace at 870 nm (**Figure 6e** and **6f**). Nevertheless, we note that the broad STE emissions prevent the complete deconvolution of the FE emission kinetics, especially in 3D hollow {*en*}MAPbI$_3$ films with smaller Stokes shifts for the STE emission.

12
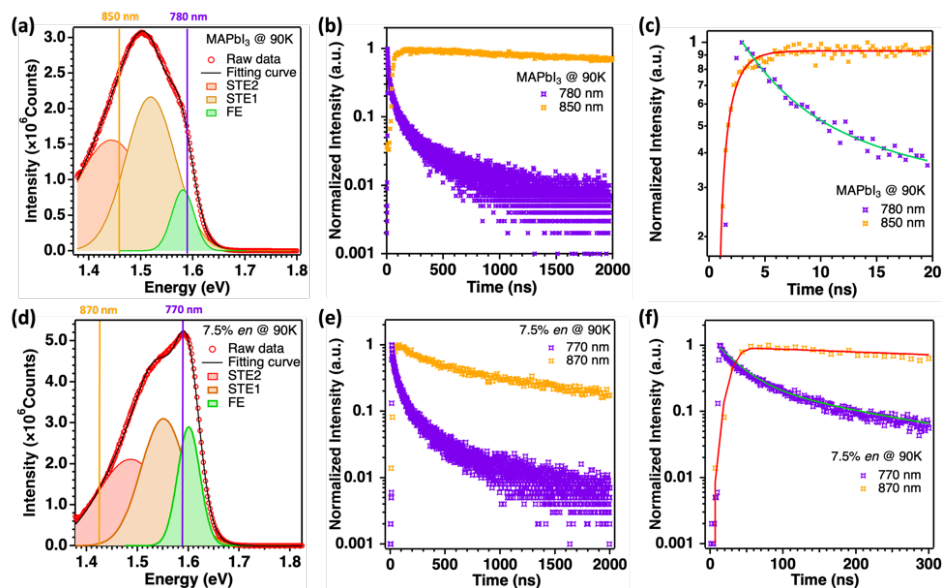
Figure 6. Steady-state PL spectra of (a) pristine MAPbI₃ and (d) {*en*}MAPbI₃ film with 7.5% *en* loading, measured at 90 K using 510 nm excitation. (b-c) (e-f) For each sample, the time-resolved PL traces were monitored at two wavelengths to track the FE and STE emissions, respectively.

▪ CONCLUSION

This study demonstrates that *en* cation incorporation significantly modifies the structural, phase transition, and photophysical properties of {*en*}MAPbI₃ thin films. The incorporation of *en* cations not only expands the perovskite unit cell but also interrupts dipole-dipole interactions among A-site cations. Experimental results reveal that increasing *en* content suppresses the tetragonal-to-orthorhombic phase transition and disrupts the collective motion of MA⁺ cations, which is pivotal for self-trapped exciton (STE) stabilization and phase behavior at low temperatures. These findings emphasize the critical role of A-site cation dipole dynamics in governing phase transitions and excitonic properties in hybrid halide perovskites. By understanding and controlling these dynamics, {*en*}MAPbI₃ emerges as a promising material for optoelectronic applications requiring stable and tunable emission properties. This work provides a foundation for the rational design of perovskite-based devices with improved stability and enhanced functionality.

▪ SUPPORTING INFORMATION

Optimized synthesis procedure for 3D hollow {*en*}MAPbI₃ films that are free of quasi-2D MAPbI₃ domains; PXRD pattern, room-temperature steady-state and time-resolved PL of the 10%

13

en(CP) film; temperature-dependent PL of the 10% *en*(CP) film; temperature evolution of XRD peak positions measured from pristine MAPbI$_3$ and 10% *en*(CP)

- ▪ **ACKNOWLEDGMENTS**

- ▪ **REFERENCE**

(1) Chen, T.; Chen, W.-L.; Foley, B. J.; Lee, J.; Ruff, J. P.; Ko, J. P.; Brown, C. M.; Harriger, L. W.; Zhang, D.; Park, C. Origin of long lifetime of band-edge charge carriers in organic–inorganic lead iodide perovskites. *PNAS* **2017**, *114* (29), 7519-7524.

(2) Green, M. A.; Jiang, Y.; Soufiani, A. M.; Ho-Baillie, A. Optical properties of photovoltaic organic–inorganic lead halide perovskites. *J. Phys. Chem. Lett.* **2015**, *6* (23), 4774-4785.

(3) Xu, J.; Maxwell, A.; Wei, M.; Wang, Z.; Chen, B.; Zhu, T.; Sargent, E. H. Defect tolerance of mixed B-site organic–inorganic halide perovskites. *ACS Energy Lett.* **2021**, *6* (12), 4220-4227.

(4) Zhou, Y.; Poli, I.; Meggiolaro, D.; De Angelis, F.; Petrozza, A. Defect activity in metal halide perovskites with wide and narrow bandgap. *Nature Reviews Materials* **2021**, *6* (11), 986-1002.

(5) Kim, G. W.; Petrozza, A. Defect tolerance and intolerance in metal-halide perovskites. *Adv. Energy Mater.* **2020**, *10* (37), 2001959.

(6) Jeong, M. J.; Moon, C. S.; Lee, S.; Im, J. M.; Woo, M. Y.; Lee, J. H.; Cho, H.; Jeon, S. W.; Noh, J. H. Boosting radiation of stacked halide layer for perovskite solar cells with efficiency over 25%. *Joule* **2023**, *7* (1), 112-127.

(7) Jiang, Q.; Tong, J.; Xian, Y.; Kerner, R. A.; Dunfield, S. P.; Xiao, C.; Scheidt, R. A.; Kuciauskas, D.; Wang, X.; Hautzinger, M. P. Surface reaction for efficient and stable inverted perovskite solar cells. *Nature* **2022**, *611* (7935), 278-283.

(8) Zhao, Y.; Ma, F.; Qu, Z.; Yu, S.; Shen, T.; Deng, H.-X.; Chu, X.; Peng, X.; Yuan, Y.; Zhang, X. Inactive (PbI$_2$)$_2$RbCl stabilizes perovskite films for efficient solar cells. *Science* **2022**, *377* (6605), 531-534.

(9) Zhang, B.; Liao, Y.; Tong, L.; Yang, Y.; Wang, X. Ion migration in Br-doped MAPbI$_3$ and its inhibition mechanisms investigated via quantum dynamics simulations. *Phys. Chem. Chem. Phys.* **2020**, *22* (15), 7778-7786.

(10) Akbulatov, A. F.; Luchkin, S. Y.; Frolova, L. A.; Dremova, N. N.; Gerasimov, K. L.; Zhidkov, I. S.; Anokhin, D. V.; Kurmaev, E. Z.; Stevenson, K. J.; Troshin, P. A. Probing the intrinsic thermal and photochemical stability of hybrid and inorganic lead halide perovskites. *J. Phys. Chem. Lett.* **2017**, *8* (6), 1211-1218.

(11) Park, B. w.; Seok, S. I. Intrinsic instability of inorganic–organic hybrid halide perovskite materials. *Adv. Mater.* **2019**, *31* (20), 1805337.

(12) Lanzetta, L.; Aristidou, N.; Haque, S. A. Stability of lead and tin halide perovskites: the link between defects and degradation. *J. Phys. Chem. Lett.* **2020**, *11* (2), 574-585.

(13) Jayanthi, K.; Spanopoulos, I.; Zibouche, N.; Voskanyan, A. A.; Vasileiadou, E. S.; Islam, M. S.; Navrotsky, A.; Kanatzidis, M. G. Entropy Stabilization Effects and Ion Migration in 3D "Hollow" Halide Perovskites. *J. Am. Chem. Soc.* **2022**, *144* (18), 8223-8230.

(14) Ke, W.; Stoumpos, C. C.; Zhu, M.; Mao, L.; Spanopoulos, I.; Liu, J.; Kontsevoi, O. Y.; Chen, M.; Sarma, D.; Zhang, Y. Enhanced photovoltaic performance and stability with a new type of hollow 3D perovskite {en}FASnI$_3$. *Sci. Adv.* **2017**, *3* (8), e1701293.

(15) Spanopoulos, I.; Hadar, I.; Ke, W.; Guo, P.; Mozur, E. M.; Morgan, E.; Wang, S.; Zheng, D.; Padgaonkar, S.; Manjunatha Reddy, G. N.; et al. Tunable Broad Light Emission from 3D "Hollow" Bromide Perovskites through Defect Engineering. *J. Am. Chem. Soc.* **2021**, *143* (18), 7069-7080.

(16) Spanopoulos, I.; Ke, W.; Stoumpos, C. C.; Schueller, E. C.; Kontsevoi, O. Y.; Seshadri, R.; Kanatzidis, M. G. Unraveling the Chemical Nature of the 3D "Hollow" Hybrid Halide Perovskites. *J. Am. Chem. Soc.* **2018**, *140* (17), 5728-5742.

(17) Grater, L.; Wang, M.; Teale, S.; Mahesh, S.; Maxwell, A.; Liu, Y.; Park, S. M.; Chen, B.; Laquai, F.; Kanatzidis, M. G. Sterically Suppressed Phase Segregation in 3D Hollow Mixed-Halide Wide Band Gap Perovskites. *J. Phys. Chem. Lett.* **2023**, *14* (26), 6157-6162.

(18) Ke, W.; Spanopoulos, I.; Tu, Q.; Hadar, I.; Li, X.; Shekhawat, G. S.; Dravid, V. P.; Kanatzidis, M. G. Ethylenediammonium-based "hollow" Pb/Sn perovskites with ideal band gap yield solar cells with higher efficiency and stability. *J. Am. Chem. Soc.* **2019**, *141* (21), 8627-8637.

(19) Ke, W.; Stoumpos, C. C.; Spanopoulos, I.; Mao, L.; Chen, M.; Wasielewski, M. R.; Kanatzidis, M. G. Efficient lead-free solar cells based on hollow {en}MASnI$_3$ perovskites. *J. Am. Chem. Soc.* **2017**, *139* (41), 14800-14806.

(20) Ke, W.; Stoumpos, C. C.; Spanopoulos, I.; Chen, M.; Wasielewski, M. R.; Kanatzidis, M. G. Diammonium cations in the FASnI$_3$ perovskite structure lead to lower dark currents and more efficient solar cells. *ACS Energy Lett.* **2018**, *3* (7), 1470-1476.

(21) Leblanc, A.; Mercier, N.; Allain, M.; Dittmer, J.; Fernandez, V.; Pauporté, T. Lead-and Iodide-Deficient (CH$_3$NH$_3$)PbI$_3$ (d-MAPI): The Bridge between 2D and 3D Hybrid Perovskites. *Angew. Chem. Int. Ed.* **2017**, *56* (50), 16067-16072.

(22) Lu, J.; Jiang, L.; Li, W.; Li, F.; Pai, N. K.; Scully, A. D.; Tsai, C. M.; Bach, U.; Simonov, A. N.; Cheng, Y. B. Diammonium and monoammonium mixed-organic-cation perovskites for high performance solar cells with improved stability. *Adv. Energy Mater.* **2017**, *7* (18), 1700444.

(23) Tsai, C.-M.; Lin, Y.-P.; Pola, M. K.; Narra, S.; Jokar, E.; Yang, Y.-W.; Diau, E. W.-G. Control of crystal

structures and optical properties with hybrid formamidinium and 2-hydroxyethylammonium cations for mesoscopic carbon-electrode tin-based perovskite solar cells. *ACS Energy Lett.* **2018**, *3* (9), 2077-2085.

(24) Fu, Y.; Hautzinger, M. P.; Luo, Z.; Wang, F.; Pan, D.; Aristov, M. M.; Guzei, I. A.; Pan, A.; Zhu, X.; Jin, S. Incorporating large A cations into lead iodide perovskite cages: Relaxed goldschmidt tolerance factor and impact on exciton–phonon interaction. *ACS Cent. Sci.* **2019**, *5* (8), 1377-1386.

(25) Li, X.; Kepenekian, M.; Li, L.; Dong, H.; Stoumpos, C. C.; Seshadri, R.; Katan, C.; Guo, P.; Even, J.; Kanatzidis, M. G. Tolerance factor for stabilizing 3D hybrid halide perovskitoids using linear diammonium cations. *J. Am. Chem. Soc.* **2022**, *144* (9), 3902-3912.

(26) Ke, W.; Spanopoulos, I.; Tu, Q.; Hadar, I.; Li, X.; Shekhawat, G. S.; Dravid, V. P.; Kanatzidis, M. G. Ethylenediammonium-Based "Hollow" Pb/Sn Perovskites with Ideal Band Gap Yield Solar Cells with Higher Efficiency and Stability. *J. Am. Chem. Soc.* **2019**, *141* (21), 8627-8637.

(27) Ke, W.; Stoumpos, C. C.; Spanopoulos, I.; Mao, L.; Chen, M.; Wasielewski, M. R.; Kanatzidis, M. G. Efficient Lead-Free Solar Cells Based on Hollow {en}MASnI$_3$ Perovskites. *J. Am. Chem. Soc.* **2017**, *139* (41), 14800-14806.

(28) Ke, W.; Stoumpos, C. C.; Zhu, M.; Mao, L.; Spanopoulos, I.; Liu, J.; Kontsevoi, O. Y.; Chen, M.; Sarma, D.; Zhang, Y.; et al. Enhanced photovoltaic performance and stability with a new type of hollow 3D perovskite {en}FASnI$_3$. *Sci. Adv.* **2017**, *3*.

(29) Al-Kahtani, A.; Tabassum, S.; Raya, I.; Khlewee, I.; Chupradit, S.; Davarpanah, A.; Elveny, M.; Ali, S. Influence of Different Rotations of Organic Formamidinium Molecule on Electronic and Optical Properties of FAPbBr$_3$ Perovskite. *Coatings* **2021**, *11* (11).

(30) Maheshwari, S.; Fridriksson, M. B.; Seal, S.; Meyer, J.; Grozema, F. C. The Relation between Rotational Dynamics of the Organic Cation and Phase Transitions in Hybrid Halide Perovskites. *J. Phys. Chem. C* **2019**, *123* (23), 14652-14661.

(31) Koegel, A. A.; Mozur, E. M.; Oswald, I. W.; Jalarvo, N. H.; Prisk, T. R.; Tyagi, M.; Neilson, J. R. Correlating broadband photoluminescence with structural dynamics in layered hybrid halide perovskites. *J. Am. Chem. Soc.* **2022**, *144* (3), 1313-1322.

(32) Bonadio, A.; Sabino, F. P.; Freitas, A. L.; Felez, M. R.; Dalpian, G. M.; Souza, J. A. Comparing the cubic and tetragonal phases of MAPbI$_3$ at room temperature. *Inorg. Chem.* **2023**, *62* (19), 7533-7544.

(33) Halder, A.; Rakita, Y.; Cahen, D.; Sarkar, S. K. Effect of Low Pressure on Tetragonal to Cubic Phase Transition of Methylammonium Lead Iodide Perovskite. *J. Phys. Chem. Lett.* **2020**, *11* (4), 1473-1476.

(34) Kong, W.; Ye, Z.; Qi, Z.; Zhang, B.; Wang, M.; Rahimi-Iman, A.; Wu, H. Characterization of an abnormal photoluminescence behavior upon crystal-phase transition of perovskite CH$_3$NH$_3$PbI$_3$. *Phys. Chem. Chem. Phys.* **2015**, *17* (25), 16405-16411.

(35) Li, Y.; Song, H.; Ma, X.; Liu, J.; Ge, C.; Liu, D.; Liu, S. Observation of Tetragonal-to-Orthorhombic Phase Transition in Perovskite MAPbI$_3$ Single Crystal via Ultrafast Photoexcitation. *J. Phys. Chem. C* **2023**, *127* (26),

12613-12620.

(36) Yu, C.; Kawakita, Y.; Kikuchi, T.; Kofu, M.; Honda, T.; Zhang, Z.; Zhang, Z.; Liu, Y.; Liu, S. F.; Li, B. Atomic Structure and Dynamics of Organic–Inorganic Hybrid Perovskite Formamidinium Lead Iodide. *J. Phys. Chem. Lett.* **2024**, *15* (1), 329-338.

(37) Maheshwari, S.; Patwardhan, S.; Schatz, G. C.; Renaud, N.; Grozema, F. C. The effect of the magnitude and direction of the dipoles of organic cations on the electronic structure of hybrid halide perovskites. *Phys. Chem. Chem. Phys.* **2019**, *21* (30), 16564-16572.

(38) Mozur, E. M.; Hope, M. A.; Trowbridge, J. C.; Halat, D. M.; Daemen, L. L.; Maughan, A. E.; Prisk, T. R.; Grey, C. P.; Neilson, J. R. Cesium Substitution Disrupts Concerted Cation Dynamics in Formamidinium Hybrid Perovskites. *Chem. Mater.* **2020**, *32* (14), 6266-6277.

(39) Lee, J. H.; Lee, J.-H.; Kong, E.-H.; Jang, H. M. The nature of hydrogen-bonding interaction in the prototypic hybrid halide perovskite, tetragonal $CH_3NH_3PbI_3$. *Sci. Rep.* **2016**, *6* (1), 21687.

(40) Li, S.; Luo, J.; Liu, J.; Tang, J. Self-Trapped Excitons in All-Inorganic Halide Perovskites: Fundamentals, Status, and Potential Applications. *J. Phys. Chem. Lett.* **2019**, *10* (8), 1999-2007.

(41) Xu, Z.; Jiang, X.; Cai, H.-p.; Chen, K.; Yao, X.; Feng, Y. Toward a general understanding of exciton self-trapping in metal halide perovskites. *J. Phys. Chem. Lett.* **2021**, *12* (43), 10472-10478.

(42) Tan, J.; Li, D.; Zhu, J.; Han, N.; Gong, Y.; Zhang, Y. Self-trapped excitons in soft semiconductors. *Nanoscale* **2022**, *14* (44), 16394-16414.

(43) Wu, C.; Chen, K.; Guo, D.; Wang, S.; Li, P. Cations substitution tuning phase stability in hybrid perovskite single crystals by strain relaxation. *RSC Adv.* **2018**, *8* (6), 2900-2905.

(44) Phuong, L. Q.; Yamada, Y.; Nagai, M.; Maruyama, N.; Wakamiya, A.; Kanemitsu, Y. Free Carriers versus Excitons in CH3NH3PbI3 Perovskite Thin Films at Low Temperatures: Charge Transfer from the Orthorhombic Phase to the Tetragonal Phase. *J. Phys. Chem. Lett.* **2016**, *7*, 2316-2321.

(45) Chen, Q.; De Marco, N. Y.(Michael) Yang, T. B. Song, C.-C. Chen, H. Zhao, Z. Hong, H. Zhou, Y. Yang, *Nano Today* **2015**, *10*, 355.

(46) Baloch, A. A.; Alharbi, F. H.; Grancini, G.; Hossain, M. I.; Nazeeruddin, M. K.; Tabet, N. Analysis of photocarrier dynamics at interfaces in perovskite solar cells by time-resolved photoluminescence. *J. Phys. Chem. C* **2018**, *122* (47), 26805-26815.

(47) Kong, L.; Liu, G.; Gong, J.; Hu, Q.; Schaller, R. D.; Dera, P.; Zhang, D.; Liu, Z.; Yang, W.; Zhu, K. Simultaneous band-gap narrowing and carrier-lifetime prolongation of organic–inorganic trihalide perovskites. *PNAS* **2016**, *113* (32), 8910-8915.

(48) Wright, A. D.; Verdi, C.; Milot, R. L.; Eperon, G. E.; Pérez-Osorio, M. A.; Snaith, H. J.; Giustino, F.; Johnston, M. B.; Herz, L. M. Electron–phonon coupling in hybrid lead halide perovskites. *Nat. Comm.* **2016**, *7* (1), 11755.

(49) Steele, J. A.; Puech, P.; Keshavarz, M.; Yang, R.; Banerjee, S.; Debroye, E.; Kim, C. W.; Yuan, H.; Heo, N. H.; Vanacken, J. Giant electron–phonon coupling and deep conduction band resonance in metal halide double perovskite. *ACS Nano* **2018**, *12* (8), 8081-8090.

(50) Herz, L. M. Charge-carrier dynamics in organic-inorganic metal halide perovskites. *Annu. Rev. Phys. Chem.* **2016**, *67* (1), 65-89.

(51) D'innocenzo, V.; Grancini, G.; Alcocer, M. J.; Kandada, A. R. S.; Stranks, S. D.; Lee, M. M.; Lanzani, G.; Snaith, H. J.; Petrozza, A. Excitons versus free charges in organo-lead tri-halide perovskites. *Nat. Comm.* **2014**, *5* (1), 3586.

(52) Ambrosio, F.; Mosconi, E.; Alasmari, A. A.; Alasmary, F. A. S.; Meggiolaro, D.; De Angelis, F. Formation of Color Centers in Lead Iodide Perovskites: Self-Trapping and Defects in the Bulk and Surfaces. *Chem. Mater.* **2020**, *32* (16), 6916-6924.

Collective Motion of Methylammonium Cations Affects Phase Transition and Self-Trapped Exciton Emission in MAPbI$_3$ Films

Chia-Hsun Yeh,[1] Wen-Yu Cheng,[2] Tai-Che Chou,[1] Yi-Chun Liu,[1] Chia-Wei Chang,[1] Yu-Sheng Chen,[3] Chih-Hsing Wang,[1] Shih-Chang Weng,[3] Ian D. Sharp,[2,] Pi-Tai Chou,[1,4] Chang-Ming Jiang[1,4,*]*

[1]Department of Chemistry, National Taiwan University, 10617 Taipei, Taiwan

[2]Walter Schottky Institute, Technical University of Munich, 85748 Garching, Germany

[3]National Synchrotron Radiation Research Center, 300092 Hsinchu, Taiwan

[4]Center for Emerging Materials and Advanced Devices, National Taiwan University, 10617 Taipei, Taiwan

*Corresponding Authors: sharp@wsi.tum.de, cmjiang@ntu.edu.tw

Synthesis optimization for {*en*}MAPbI₃ films
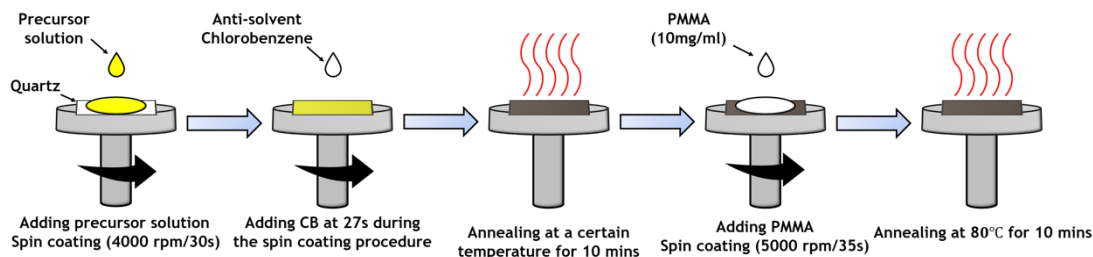
Figure S1. Schematic diagram of the one-step spin-coating procedure for synthesizing pristine and {*en*}MAPbI₃ films with a PMMA protective layer.

Initially, ethylenediammnium iodide replaced methylammonium iodide at a 1:1 ratio in the precursor solution, and the annealing temperatures used for synthesizing {*en*}MAPbI₃ were optimized. For films with 5% and 10% *en* loadings, PXRD patterns employing 80–100°C annealing temperatures for 10 minutes are presented in **Figures S2a** and **S2b**, respectively. Diffraction peaks corresponding to quai-2D MAPbI₃ emerged at 6.92, 7.55, and 9.52º when annealed at 80°C, and their intensities diminished with increasing annealing temperature. At 100°C annealing temperature, however, the appearance of a PbI₂ (001) diffraction peak at 13º indicates degradation of MAPbI₃. Therefore, 95°C was chosen for the subsequent optimization processes.
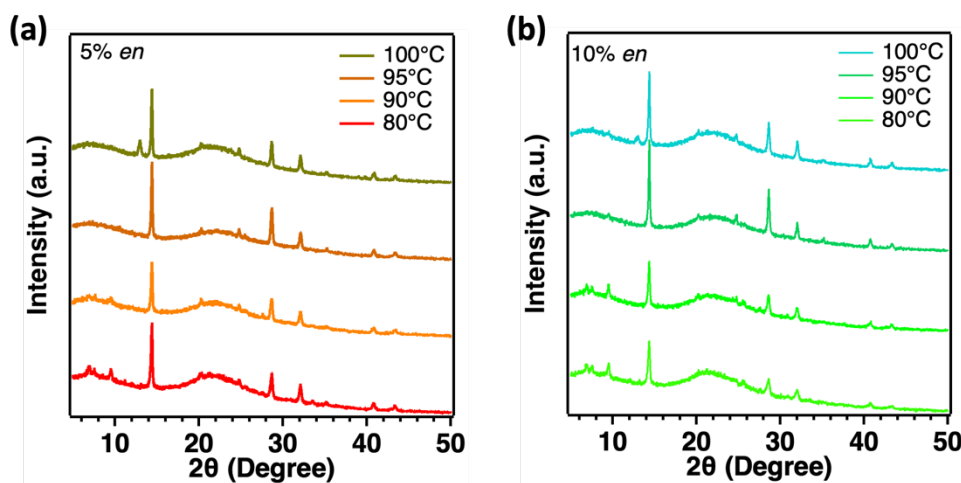
Figure S2. (a-b) PXRD patterns of {*en*}MAPbI₃ films with (a) 5% and (b) 10% *en* loadings synthesized with different annealing temperatures. Ethylenediammonium iodide replaced methylammonium iodide at a 1:1 ratio in the precursor solution.

Next, the *en*/MA⁺ replacement ratios were optimized for each *en* loading. final stage of optimization entailed assessing the influence of the *en*/MA⁺ ratio in each sample. After intentionally adding large cations into the lattice structure, removing an equivalent number of

S2

cations from the lattice was imperative to maintain overall electrical neutrality. This optimization was executed for each sample featuring varying *en* loadings, and the outcomes are illustrated in **Figure S3**. Notably, samples with different *en* loading concentrations exhibited distinct optimized *en*/MA$^+$ ratios. A discernible trend emerged, indicating that with higher *en* loadings, a larger proportion of MA$^+$ cations must be retained in the precursor solution. This trend stems from the notion that a greater loading concentration of *en* cations into the lattice structure necessitates the removal of a corresponding quantity of MA$^+$ cations to preserve the electrical neutrality of the entire crystal. However, it is imperative to strike a balance, as an excessively low concentration of MA$^+$ cations may jeopardize the integrity of the crystal's 3D framework. Consequently, the MA$^+$ concentration in the precursor solution must be augmented proportionally with increases in the *en* loading concentration.
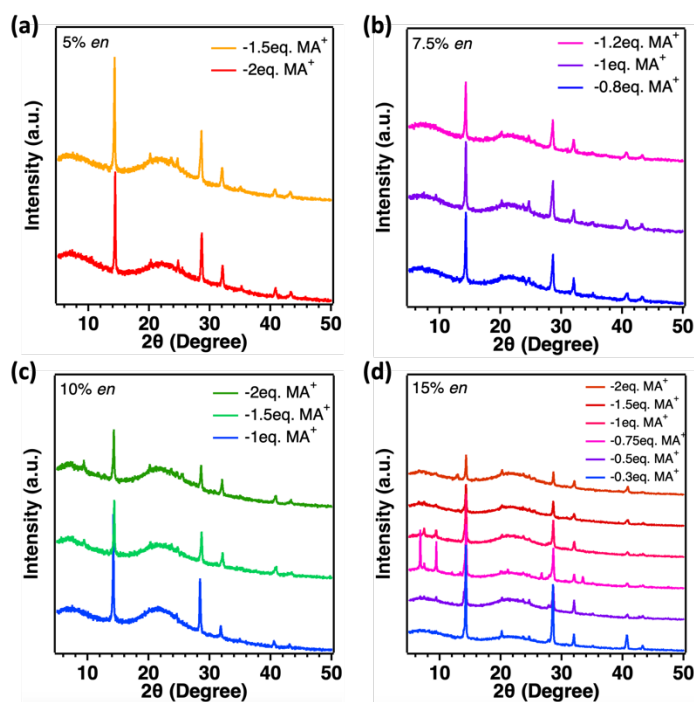
Figure S3. PXRD patterns of {*en*}MAPbI$_3$ films with (a) 5%, (b) 7.5%, (c)10%, and (d) 15% *en* loadings employing 95°C annealing temperature and varying *en*/MA$^+$ replacement ratios.

The above statement underscores the pivotal role played by two key factors in the synthesis process: annealing temperature and *en*/MA$^+$ ratios. Consequently, we endeavored to elevate the annealing temperature in samples featuring high en^{2+} loadings while maintaining the optimized *en*/MA$^+$ ratio. The outcomes of this combined approach are depicted in **Figure S4**. Notably, for the films with 5%, 7.5%, and 15% *en* loadings, the most favorable annealing temperatures were determined to be 90°C, 95°C, and 130°C, respectively.
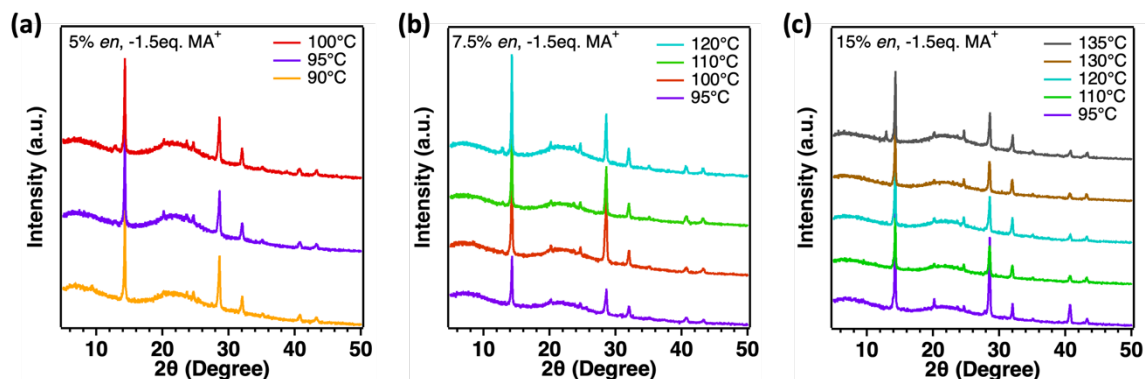
S3

Figure S4. PXRD patterns of {*en*}MAPbI₃ films (a) 5%, (b) 7.5%, and (c) 15% *en* loadings at specified *en*/MA⁺ replacement ratios using varying annealing temperatures.
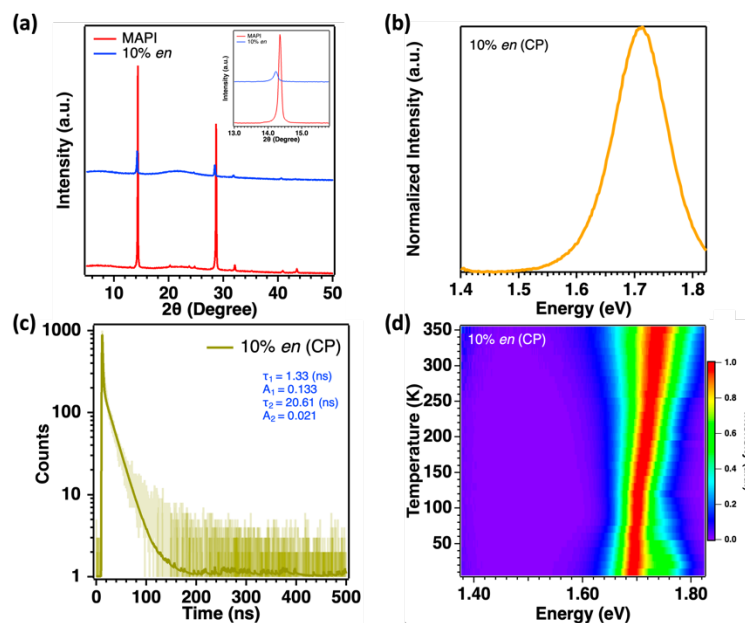

Figure S5. (a) Comparison of PXRD patterns of pristine MAPbI₃ and the {*en*}MAPbI₃ film with 10% *en* loading and crystallized into the cubic perovskite phase. (b) Room-temperature steady-state PL spectrum and (c) time-resolved PL trace monitored at 1.71 eV of the 10% *en*(CP) film. (d) Temperature-dependent PL spectra of the 10% *en*(CP) film.

In conclusion, the optimization of the synthesis process hinges on two crucial variables: the annealing temperature and the *en*/MA⁺ ratio in each sample. The annealing temperature governs the thermal energy imparted to the sample, with higher temperatures resulting in higher-quality thin films exhibiting a 3D hollow structure. However, excessively elevated annealing temperatures may lead to the diffusion of MA⁺ cations, potentially causing sample degradation. To counteract

S4

this, an excess of MA^+ is introduced into the precursor solution to compensate for any loss during annealing. Consequently, each thin film sample with a different *en* loading concentration possesses its own optimized *en*/MA^+ ratio.
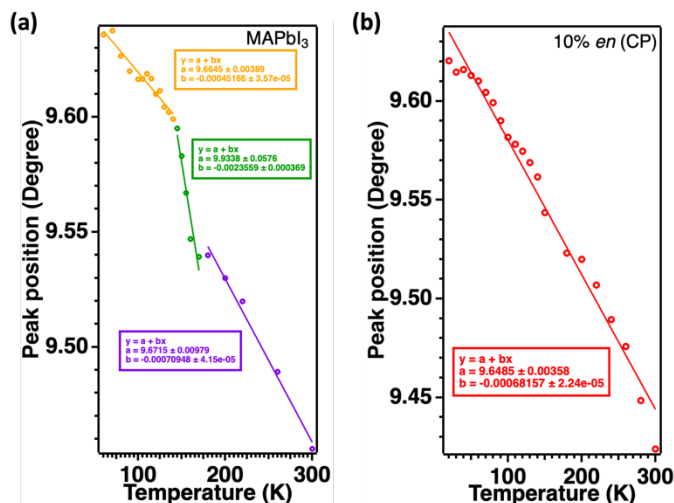
Temperature-dependent PXRD measurements

Figure S6. Temperature-dependent diffraction peak positions of (a) pristine MAPbI₃ film and (b) 10% *en*(CP) film.
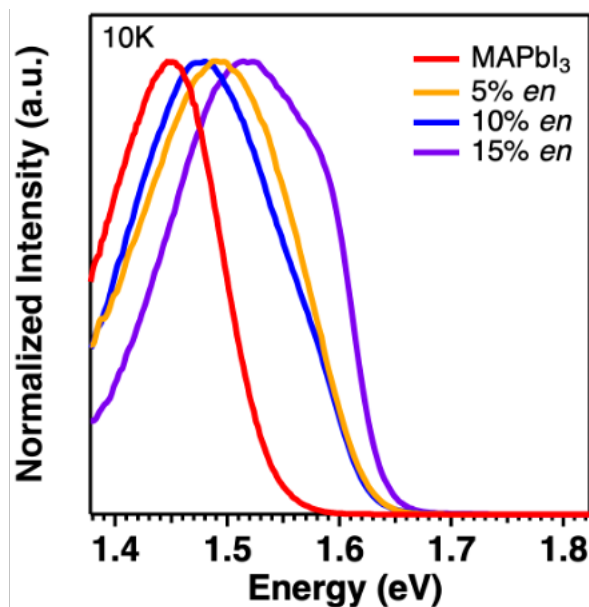

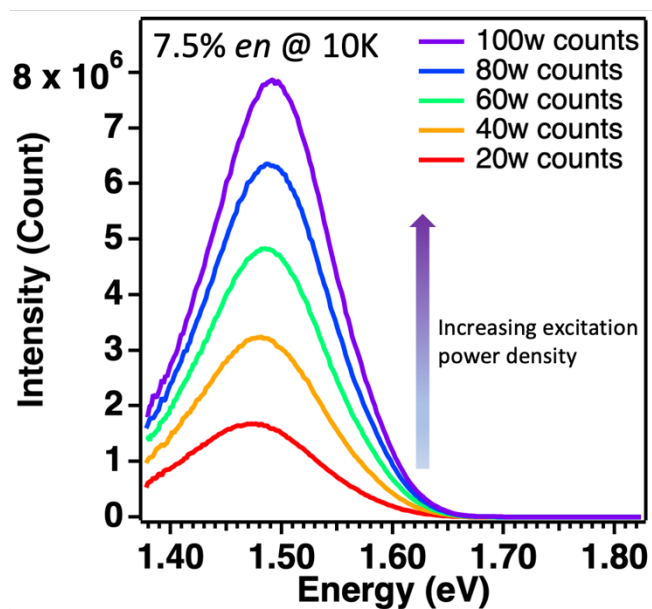**Figure S7.** PL spectra of {*en*}MAPbI₃ thin films with 0-15% *en* loading at 10K.

Figure S8. Steady-state PL spectra measured from a {en}MAPbI₃ film with 7.5% *en* loading at 10 K using different excitation powers from a 510 nm laser.